Engineering Applications of Computational Fluid Mechanics Vol. 5, No. 1, pp. 117–126 (2011)

IMPLEMENTATION AND APPLICATION OF THE LATTICE BOLTZMANN METHOD USING MATLAB

Jérôme Guiet*, Marcelo Reggio and Alberto Teyssedou

École Polytechnique de Montréal, Campus de l'Université de Montréal, 2500 chemin du Polytechnique Montréal, Québec H3T 1J4, Canada
** Email: jerome.guiet@polymtl.ca (Correspondence Author)*

ABSTRACT: The Bhatnagar-Gross-Krook version of the Lattice Boltzmann method on two-dimensional Cartesian meshes has been used to develop a computational program suitable for the Matlab environment. The basic algorithm is implemented with a grid refinement approach that includes an accurate boundary treatment to handle complex geometries in the lattice Boltzmann framework. Validation of the program was conducted on a steady flow over a staggered bundle of tubes for which data are available. After this preliminary step, the code was applied to the calculation of the characteristic aerodynamic parameters at steady state around clean and three ice-accreted NACA63-415 profiles at $\mathrm{Re} = 500$ at $\alpha = 0°$ and $8°$. Finally, the unsteady nature of the method was used to compute flows over this clean and ice-accreted airfoil for an angle of attack of $\alpha = 28°$. For all configurations, results were compared with computational results carried out with the commercial package fluent.

Keywords: lattice Boltzmann, ice-accreted profile, two-dimensional, separated flows, unsteady flows

1. INTRODUCTION

The lattice Boltzmann method (LBM) (Succi, 2001), built on the Boltzmann equation and historically derived from the Lattice Gas Cellular Automata (LGCA) methods (Wolf-Gladrow, 2000), is an emerging alternative to the Navier-Stokes (NS) based methods for the simulation of fluid flows. The motivations for its use are both theoretical and practical. On the one hand, the LBM provides a novel perspective on complex physical systems based on the averaged microscopic properties of fluids. It makes possible the expression of a wide range of macroscopic flows which are ultimately representative of similar molecular states. With its mesoscopic definition through the lattice Bhatnagar-Gross-Krook (BGK) model it also shows exact conservation properties (Bhatnagar, 1954; Chen et al., 1991; Koelman, 1991; Qian et al., 1992). On the other hand, despite its microscopic foundation, the method is easy to implement, flexible towards additional physics, and advantageous for parallelization.

Based on this theory, which concentrates on the calculation of particle distribution functions instead of macroscopic flow variables, a 2D computational program was developed. A first fundamental validation step of the current implementation was conducted for a cross-flow in a staggered bundle of tubes for which numerical data are available.

After this step, steady flows around three sections of an ice-accreted blade were simulated. The basic profile is a NACA63-415 used in wind turbines and ice conditions correspond to three sections at different radial positions. Lift and drag coefficients were calculated for angles of $\alpha = 0°$ and $8°$ for both clean and ice-accreted profiles. The goal of these simulations is to confirm the ability of the model to calculate the flow around complex shapes, like airfoils modified by ice accretion, despite the use of Cartesian meshes.

After these steady state calculations, computations of the unsteady flow for clean and ice-accreted conditions over the NACA63-415 airfoil for an angle of attack of $\alpha = 28°$ were also conducted to assess the performance of the method for handling this kind of separated flow.

For all cases, comparisons with Navier-Stokes solutions obtained with commercial finite volume package FLUENT were carried out.

2. THE LATTICE-BGK METHOD

2.1 Basic concept

Developed two decades ago, the LBM examines the molecular state of fluids instead of the classical macroscopic level to conduct flow simulations (Succi, 2001; Wolf-Gladrow, 2000). The so-called lattice-BGK (LBGK) variant of the LBM introduced by Chen et al. (1991), Koelman (1991), and Qian et al. (1992), is used in this study. The LBGK method is a discrete solution of the

Received: 1 Apr. 2010; Revised: 27 Aug. 2010; Accepted: 3 Oct. 2010

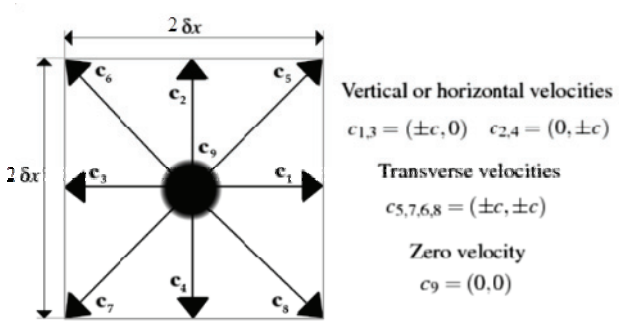

Fig. 1 Discrete phase space in two dimensions, (D2Q9 lattice).

Boltzmann transport equation for particle distribution functions on a simplified phase space (He and Luo, 1997). Usually, this space is represented by a Cartesian lattice.

In the current work, the 2D discretization, known as the D2Q9 lattice, sketched in Fig. 1, has been adopted.

With such a type of discretization, molecules are considered like sets of particles expressed by discrete distribution functions f_i. These move on the lattice from cells to cells along nine directions $i=1$ to 9, with constant molecular speeds $\boldsymbol{c}_i$ proportional to a constant lattice velocity $c=\delta x/\delta t$, where δx and δt are the lattice grid spacing and time step. On the D2Q9 lattice (Fig. 1) these nine velocities $\boldsymbol{c}_i$ along nine directions are eight phase space discretization velocities and a ninth with zero speed $\boldsymbol{c}_9$.

Additionally, Accordingly, the evaluation of the moving particle distribution functions $f_i(\boldsymbol{x},t)$ following the discrete molecular speed $\boldsymbol{c}_i$ is written as:

$$f_i(\boldsymbol{x}+\boldsymbol{c}_i\delta t, t+\delta t) = f_i(\boldsymbol{x},t)+\frac{1}{\tau}\left(f_i^{eq}(\boldsymbol{x},t)-f_i(\boldsymbol{x},t)\right) \quad (1)$$

The last term represents the BGK collision that accounts for the variation of the number of particles moving in each direction on the lattice due to microscopic inter-particle collisions (Bhatnagar, 1954). These collisions are embedded in a relaxation time τ which is linked to the kinematic viscosity ν by:

$$\nu=\frac{\delta t\, c^2}{3}\left(\tau-\frac{1}{2}\right) \quad (2)$$

In order to keep a positive viscosity and to guarantee numerical stability, $\tau>1/2$ is required. The equilibrium distribution f_i^{eq} appearing in Eq. (1) corresponds to an ideal state to which the particle distribution functions tend to a specific macroscopic state. This is derived from a Maxwellian distribution function and is expressed in terms of macroscopic flow characteristics under a low-Mach assumption $Ma=\|\boldsymbol{u}\|/c_s\le 0.1$, where $c_s=c/\sqrt{3}$, to ensure incompressibility:

$$f_i^{eq}(\rho,\boldsymbol{u})=\rho w_i\left(1+\frac{3}{c^2}\boldsymbol{c}_i\cdot\boldsymbol{u}+\frac{9}{2c^4}(\boldsymbol{c}_i\cdot\boldsymbol{u})^2-\frac{3}{2c^2}\boldsymbol{u}^2\right) \quad (3)$$

where ρ is the macroscopic density of the fluid, $\boldsymbol{u}$ the aforementioned macroscopic flow velocity, and w_i weighting factors that depend on the lattice and the mesoscopic velocities $\boldsymbol{c}_i$. For the D2Q9 lattice the parameters w_i are given as:

$$w_{i=1,2,3,4}=\frac{1}{4},\quad w_{i=5,6,7,8}=\frac{1}{36}\quad\text{and}\quad w_{i=9}=\frac{4}{9} \quad (4)$$

At each time step, from the distribution functions at a mesoscopic level, the macroscopic moments for the hydrodynamic pressure P and for the velocity $\boldsymbol{u}$ are approximated as:

$$\sum_i f_i(\boldsymbol{x},t)=\rho(\boldsymbol{x},t)=\frac{P(\boldsymbol{x},t)}{c_s^2} \quad (5)$$

$$\sum_i f_i(\boldsymbol{x},t)\, c_{i,\alpha}=\rho(\boldsymbol{x},t)\, u_\alpha \quad (6)$$

The set of equations Eqs. (1-6), with a specific boundary treatment, enables to simulate the evolution of flows in the lattice Boltzmann framework. For simplicity we chose $\delta x=\delta t$ such that $c=1$. We also consider the simulations in lattice units such that $\delta x=1\,lu$ and $\delta t=1\,lt$.

2.2 Boundary conditions

Like any computational method used for flow simulation, the treatment of the boundary conditions (BC) is a sensitive part of the method, because BC's are often the sources of inaccuracy and instability. The aim behind this aspect of the problem consists of defining a mesoscopic state on the boundary by knowing the macroscopic flow conditions, or knowing the mesoscopic state at the boundary. Different types of BC's have been developed (Succi, 2001; Latt et al., 2008). The first that we have selected is the halfway bounceback along solid walls, where all incident distribution functions along the wall are sent back to the flow domain such that $f_i(\boldsymbol{x},t+\delta t)=f_{-i}(\boldsymbol{x},t)$ with $\boldsymbol{c}_{-i}=-\boldsymbol{c}_i$. This BC is very simple, but curved boundaries are only approximated by series of

stairs, thereby inducing inaccuracies. The second BC used in this work makes it possible to set a macroscopic conditions through specific distributions $f_{i,\,Bound}$, in such a way that they are simply replaced with the corresponding equilibrium distribution functions Eq. (3): $f_{i,\,Bound} = f_i^{eq}\left(\rho_{Bound}, \boldsymbol{u}_{Bound}\right)$. This technique is used to impose either a velocity at the inlet $\boldsymbol{u}_{Bound}$, a density at the outlet ρ_{Bound} or a symmetric boundary.

Regarding the initial conditions, a unit density and a zero velocity are applied throughout the computational domain using the equilibrium distributions.

2.3 Grid refinement and curved boundary treatment

The LBGK method and especially the key equation, Eq. (1), are explicit, easy to implement, and straightforward to parallelize, but were devised to be used with a regular lattice structure having a uniform spacing. This imposes a challenge over the whole domain, that consists of obtaining a high resolution discretization near an airfoil without wasting simulation time, because fine lattices would be required everywhere. This resolution dilemma is increased due to the location of the inlet and outlet boundaries, which must be placed far away to limit its influence close to the body field.

An approach to solve such a quandary is to divide the computational domain into a number of grid blocks such that in each block a different lattice spacing can be used. Several studies addressing this multi-block technique for the LBGK method have been conducted (Filippova and Hänel, 1998; Rohde et al., 2006). In order to efficiently tackle the NACA airfoils, we have adopted the technique of Dupuis and Chopard (2003), that provides an accurate and conservative interface treatment between neighbouring blocks satisfying the continuity of mass, momentum, and stress. With this multi-block technique, the flow domain is divided into several Cartesian meshes of different sizes, along with a discretization factor $m = \delta x_{coarse} / \delta x_{fine}$. In order to respect the global viscosity in the different domains, involving different lattice sizes, the definition of the characteristic relaxation time, τ_{fine} and τ_{coarse}, between two levels must obey the following rule:

$$\tau_{fine} = \frac{1}{2} + m\left(\tau_{coarse} - \frac{1}{2}\right) \tag{7}$$

To conduct simulations with the multi-block technique, the evolution of particle distribution functions is applied independently on each sub lattice, with the specific relationship given by Eq. (7). At the same time step, a special data transfer, from coarse to fine grids and from fine to coarse grids, is enforced as given by the following equations:

$$f_i^{fine} = f_i^{eq} + \frac{\tau_{fine}}{m\,\tau_{coarse}}\left(f_i^{coarse} - f_i^{eq}\right) \tag{8}$$

$$f_i^{coarse} = f_i^{eq} + \frac{m\,\tau_{coarse}}{\tau_{fine}}\left(f_i^{fine} - f_i^{eq}\right) \tag{9}$$

The missing distribution functions on interfacial nodes are then spatially and temporally interpolated between these known distributions to complete the interconnection between meshes. This idea is illustrated in Fig. 2. A second way to improve the accuracy of the LBGK method, while keeping Cartesian lattices on the boundaries, is a special treatment of curved BC. In addition to the multi-block method an improvement of the classical bounceback approach was applied. This procedure, provided by Mei et al. (1999), allows irregularities generated by the regular Cartesian mesh of the lattice to be smoothed out. Further, this technique enables the correct position of the boundaries to be considered. Actually a specific treatment of the streaming distribution functions is applied along boundary nodes according to the distance Δ between fluid nodes and the wall of the profile (Fig. 3):

$$\Delta = \frac{\left|\boldsymbol{x}_F - \boldsymbol{x}_W\right|}{\left|\boldsymbol{x}_F - \boldsymbol{x}_S\right|} \tag{10}$$

In this expression, the index F, W, and S denote fluid, wall, and solid respectively. The post-collision distribution functions f_i moving from a fluid node to a wall node are sent back to the fluid node following a second-order accurate treatment. Fig. 3 and Eqs. (11-14) respectively illustrate and describe the relations between parameters that make it possible to complete the bounceback between two time steps along a curved boundary:

$$\begin{aligned} &f_{\bar{i}}(\boldsymbol{x}_S + \boldsymbol{c}_{\bar{i}}\delta t, t+\delta t) \\ &= (1-\chi) f_i(\boldsymbol{x}_F, t) + \chi f_i^{(*)}(\boldsymbol{x}_S, t) - 2w_i\rho\frac{3}{c^2}\left(\boldsymbol{c}_i \cdot \boldsymbol{u}_W\right) \end{aligned} \tag{11}$$

with fictitious distribution functions given by:

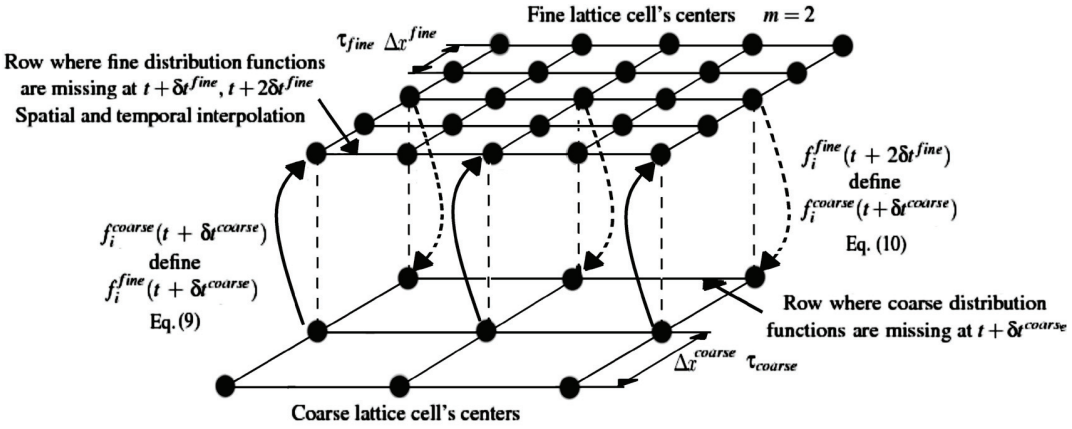

Fig. 2 Interface structure between two blocks of different lattice spacing, $m = 2$.

$$f_i^{(*)}(\boldsymbol{x}_S,t) = \rho(\boldsymbol{x}_F,t)\, w_i\left(1+\frac{3}{c^2}\boldsymbol{c}_i\cdot\boldsymbol{u}_{SF}+\frac{9}{2c^4}\left(\boldsymbol{c}_i\cdot\boldsymbol{u}_F\right)^2-\frac{3}{2c^2}\boldsymbol{u}_F{}^2\right) \quad (12)$$

and the specific parameters:

$$\boldsymbol{u}_{SF} = \left(1-\frac{3}{2\Delta}\right)\boldsymbol{u}_F+\frac{3}{2\Delta}\boldsymbol{u}_W ,$$

$$\text{with } \chi = \frac{2(2\Delta-1)}{(2\tau+1)}, \text{ when } \Delta \geq \frac{1}{2} \quad (13)$$

$$\boldsymbol{u}_{SF} = \boldsymbol{u}_{FF}, \text{ with } \chi = \frac{2(2\Delta-1)}{(2\tau+1)}, \text{ when } \Delta < \frac{1}{2} \quad (14)$$

Both aforementioned techniques, grid refinement and accurate curved boundary treatment were incorporated into our computational program to achieve the simulation around the staggered bundle of tubes and the NACA profiles. This program was applied to evaluate the drag, lift, and pressure coefficients $\left(C_d, C_l, C_p\right)$. These parameters are defined according to reference parameters, the average inlet velocity u_{ref} , the characteristic length L_{ref} , and a reference density ρ_{ref} . Thus:

$$C_p = \frac{\left|P-P_{ref}\right|}{\frac{1}{2}u_{ref}^2\rho_{ref}} \quad (15)$$

$$C_d = \frac{\left|F_x\right|}{\frac{1}{2}u_{ref}^2 L_{ref}\rho_{ref}}, \text{ and } C_l = \frac{F_y}{\frac{1}{2}u_{ref}^2 L_{ref}\rho_{ref}} \quad (16)$$

where the evaluation of the force components, F_x and F_y is achieved at a mesoscopic level with considerations of the momentum exchange along the profile boundary as suggested by Mei et al. (2002).

3. RESULTS

Based on the theory described above, a computational program was written using Matlab. After a set of verifications based on the well-known lid-driven cavity problem and the flow over the classical backward-facing step, the following applications were conducted.

3.1 The staggered bundle of tubes

This test case considers the staggered bundle of tubes shown in Fig. 4 with a ratio $P/D = 1.5$. The Reynolds number is based on the average inlet velocity u_∞ and the diameter D of the cylinders. Full details of this test case at $\mathrm{Re} = 20$ with experimental and numerical data are given by Watteaux (2008).

The boundary conditions used for this case are: bounceback on solid walls with the improvement presented in section 2.3; fixed outlet density $(\rho_{out} = 1)$; extrapolated outlet velocity; extrapolated density and fixed parabolic velocity profile (with u_{peak} the maximum velocity and $u_\infty = 2/3\, u_{peak}$) at the inlet. The results were compared through the study of the aerodynamic coefficients, C_d and C_l with $\rho_{ref} = \rho_{out}$, $u_{ref} = u_\infty$ and $L_{ref} = D$ following Eq. (16).

Because of the presence of the walls, the flow around cylinders 2 and 6 should be locally asymmetrical and consequently, the lift should not be zero over them. It is also expected that this phenomenon will disappear as the flow progresses towards the second and third rows. Cylinders 1 and 4 should also have a lower drag than the rest because of a lesser influence of neighbouring bodies on these.

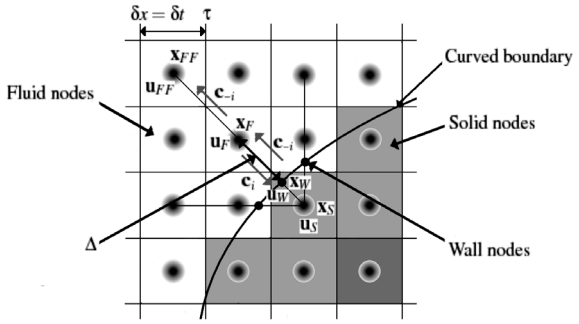

Fig. 3 Curved wall boundary on a regularly spaced lattice.

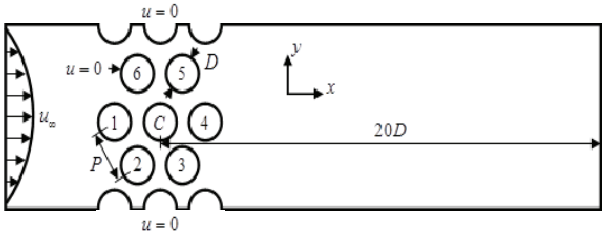

Fig. 4 Staggered bundle of tubes.

A first calculation was carried out with $lu_x = 25\ D = 1000\ lu$ and $lu_y = 207\ lu$ which denote the number of lattices along the x and y Cartesian coordinates, respectively. The simulation parameters are $u_{peak} = 0.1\ lu/lt$, $D = 40\ lu$ and the corresponding characteristic relaxation time $\tau = 0.9$.

In order to verify the grid refinement strategy and implementation presented in section 2.3, a second calculation was performed with a grid having three regions. This idea is depicted for illustration purpose in Fig. 5. The central part kept the same refinement while the inlet and outlet regions had half the number of elements in each direction ($m = 2$ between coarse and fine mesh).

Both types of discretizations led to the same results which confirmed that the refinement technique and the computer program worked properly. However, the solution did not agree with the available data. A further investigation was required to elucidate this discrepancy.

In fact, the results were roughly 50% off from the reference data. At the same time, a stronger acceleration of the flow than that given by Watteaux (2008) was found between cylinders 3 and 5 and the walls. The simulation yielded a maximum velocity of $u_{\max} = 0.34\ lu/lt$ in this region (or 3.4 times the peak velocity at the inlet), which was beyond the aforementioned limit for addressing incompressibility adequately. A second calculation was then tried on the same domain imposing an inlet velocity of $u_{peak} = 0.05\ lu/lt$ instead of $u_{peak} = 0.1\ lu/lt$. To keep the Reynolds number equal to 20, a relaxation time of $\tau = 0.7$ was used. For this new simulation the solution was substantially improved with the maximum velocity only reaching $u_{\max} = 0.14\ lu/lt$ (2.8 times u_{peak}), which is closer to the limit for considering the flow to be incompressible. This was not entirely satisfactory and a third simulation was then conducted with an inlet velocity $u_{peak} = 0.03\ lu/lt$ with a corresponding relaxation time $\tau = 0.62$ for which the maximum velocity, between cylinders 3 and 5 and the wall, reached $u_{\max} = 0.078\ lu/lt$ (2.6 times u_{peak}).

Tables 1 and 2 summarize, respectively, the set of drag and lift coefficients, computed with and without grid refinement (they match with each other) for the three different inlet velocities.

Table 1 Drag coefficients at $\mathrm{Re} = 20$ for several inlet velocities with LBGK.

Cylinder	C_d $u_{peak} = 0.1\ lu/lt$	C_d $u_{peak} = 0.05\ lu/lt$	C_d $u_{peak} = 0.03\ lu/lt$
C	35.43	24.60	23.19
1	24.65	17.86	16.89
2	34.10	24.23	22.91
3	38.44	25.62	24.07
4	18.89	12.94	12.23
5	38.44	25.62	24.07
6	34.10	24.23	22.91

Table 2 Lift coefficients at $\mathrm{Re} = 20$ for several inlet velocities with LBGK.

Cylinder	C_l $u_{peak} = 0.1\ lu/lt$	C_l $u_{peak} = 0.05\ lu/lt$	C_l $u_{peak} = 0.03\ lu/lt$
C	0	0	0
1	0	0	0
2	-0.59	-0.45	-0.47
3	-0.072	-0.0074	-0.018
4	0	0	0
5	0.072	0.0074	0.018
6	0.59	0.45	0.47

Table 3 Comparison of aerodynamic coefficients at $\mathrm{Re} = 20$.

Cylinder	C_d CADYF	C_d FLUENT	C_d LBGK	C_l CADYF	C_l FLUENT	C_l LBGK
C	23.18	23.17	23.19	0	0	0
1	16.96	16.86	16.89	0	0	0
2	22.92	22.91	22.91	-0.47	-0.38	-0.47
3	23.96	23.95	24.07	-0.0087	-0.003	-0.018
4	12.20	12.20	12.23	0	0	0
5	23.96	23.95	24.07	0.0087	0.003	0.018
6	22.92	22.91	22.91	0.47	0.38	0.47

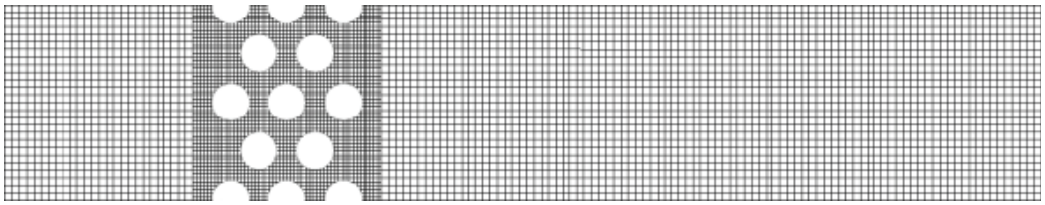

Fig. 5 Three zone grid.

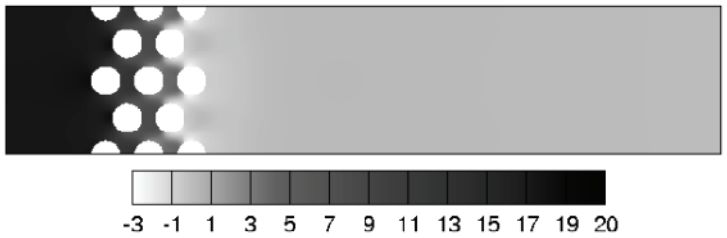

Fig. 6 Pressure distribution around the bundle of tubes at $\mathrm{Re} = 20$.

It is clear that the results heavily depend on how the incompressibility of the flow is satisfied.

Table 3 shows the most accurate results, when the inlet velocity $0.03 lu/lt$ together with coefficients obtained with the commercial software FLUENT and for this case, with data calculated using CADYF (Watteaux, 2008). This later is a very accurate and proven Navier-Stokes solver based on the finite element method that uses high order time integration (Etienne et al., 2009). The inspection of Table 3 indicates that the agreement of both aerodynamic coefficients is generally very good.

One can also underline the symmetric-antisymmetric nature of the flow as expected. The same drag coefficient is found for cylinders (2, 6) and (3, 5) while the lift parameter is virtually null for all cylinders with the exception of numbers 2 and 6, for which the flow in not symmetric around them. As expected, the drag is lower for the first and last centerline cylinders 1 and 4, respectively.

A final comparison is given considering the pressure drop between the inlet P_{in} and the outlet P_{in} (based on ρ_{in} and ρ_{out} following Eq. (16) on the centerline of the channel). Specifically, the dimensionless pressure drop given by

$$\Delta P = \frac{P_{in} - P_{out}}{\frac{1}{2}\rho_{ref} u_{ref}^2} \tag{17}$$

leads to $\Delta P = 19.5$, with $\rho_{ref} = \rho_{out}$ and $u_{ref} = u_\infty$, while the values provided by CADYF's and FLUENT softwares are $\Delta P = 19.4$ and $\Delta P = 19.9$, respectively. These results are also in good agreement. Fig. 6 illustrates the predicted pressure field.

3.2 The NACA63-415 airfoil

Following the previous test case used to verify the program that includes both multiple grid refinement and curved boundary treatment, the flow around the NACA63-415 airfoil under clean and ice-accreted conditions was then studied.

Simulations were carried out for laminar flows and for a Reynolds number limited to $\mathrm{Re} = 500$. This value is clearly low for typical aerodynamic simulations, but the basic lattice Boltzmann formulation is only suitable for low Reynolds numbers; this is due to stability issues related to the relaxation time τ. Some models and methods, however, permit turbulent flows to be treated. The most appropriate one is the LES (Large Eddy Simulation) formulation with Smagorinsky model, where turbulence can be taken into account by modifying the relaxation time τ. The LES method is more relevant for 3D flow simulations while this study only concerns 2D-flow configurations. Further, the present work is aimed to test the ability of the current LBM formulation to handle complex geometries for laminar flows. The proposed formulation is applied by using 3 levels of refinement and a factor $m = 5$ between each mesh level, as shown in Fig. 7. For a length of the profile of $C = 0.6\,m$ the chosen adimensionalized length of the airfoil on the coarse mesh is $L_{c,ref} = 12.5\,lu$ such that the length of the flow domain $lu_x = 33.6 \times L_{c,ref} = 420\,lu$ and the height $lu_y = 20 \times L_{c,ref} = 250\,lu$. Regarding the boundary conditions, a solid wall with curved boundary treatment is applied along the airfoil, a

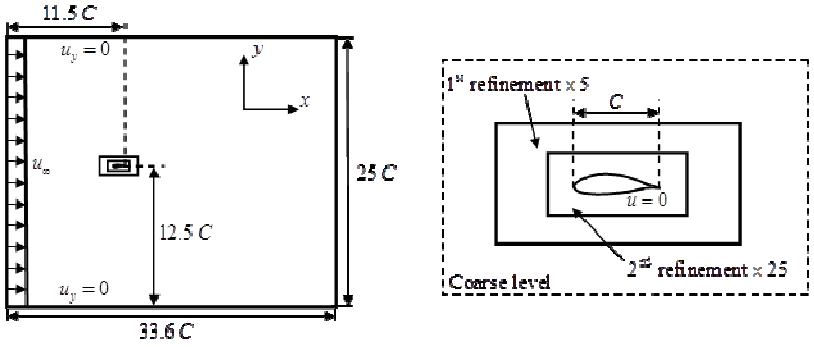

Fig. 7 Flow domain with multi-blocks approach and a refinement factor $m = 5$.

flow inlet is imposed on the left with $u_\infty = 0.1\, m/s = 0.1\, lu/lt$ and extrapolated density. For both upper and lower boundaries symmetry is considered, that is to apply opposite normal velocity with extrapolated density. Finally, at the outlet the density $\rho_{out} = 1$ is enforced and the velocity is extrapolated. The corresponding kinematic viscosity on the coarse mesh is $\nu = 1.2\,10^{-4}\ m^2/s$ and with these parameters the characteristic relaxation time becomes $\tau_c = 0.5075$.

On the first refinement the chord of the profile is then $L_{1,ref} = 5 \times L_{c,ref} = 62.5\, lu$, and following Eq. (7) the characteristic relaxation time is $\tau_1 = 0.5375$.

On the finest refinement the length of the profile is $L_{2,ref} = 5 \times L_{1,ref} = 5 \times 5 \times L_{c,ref} = 312.5\, lu$ and the characteristic relaxation time is $\tau_2 = 0.6875$.

For the ice-accreted cases different shapes were obtained from experimental studies carried out in a refrigerated wind tunnel. The particular interest in this profile consists of studying the modification of aerodynamic parameters when ice forms on the blades of wind turbines. It is known that this kind of shape variation causes significant losses in turbine performance.

In order to have an appreciation of the impact of the ice on the aerodynamic coefficients and to verify the ability of the LBGK to take into account complex geometries, calculations were first performed for the clean profile at an angle of attack of $\alpha = 0°$. The flow regime of these simulations is steady, results are thus compared through a study of the aerodynamic parameters C_p, C_d and C_l (Eqs. (15), (16)) with $u_{ref} = u_\infty$, $L_{ref} = L_{2,ref}$, ρ_{ref} the centerline inlet density and P_{ref} based on this density following Eq. (5).

First, LBGK and FLUENT C_p evaluations over clean and ice-accreted NACA63-415 airfoils along the chord are presented in Figs. 8, 9, 10 and 11. The computed C_p distribution indicates that the ice shape is well accounted for, despite the fundamental difference on the formulation and on the meshing of the two methods. Nevertheless, a closer observation indicates the presence of few spikes in the results obtained with FLUENT which do not appear in LBGK calculations. These features are only present in cases with ice accretion. It is possible that this behaviour is due to the roughness induced by the ice layer on the leading edge. It should also be noticed that unlike FLUENT, the shape of the same profile in the LBGK method is taken into account by regular Cartesian meshes. A refinement treatment around airfoil and curved boundaries is then required to improve the accuracy (section 2.3). In addition, the Cartesian discretization implies that distribution functions and macroscopic quantities are not completely known on the airfoil boundary but they only can be evaluated on nearest cells. This drawback produces a smoothing on C_p values calculated from the lattice Boltzmann method.

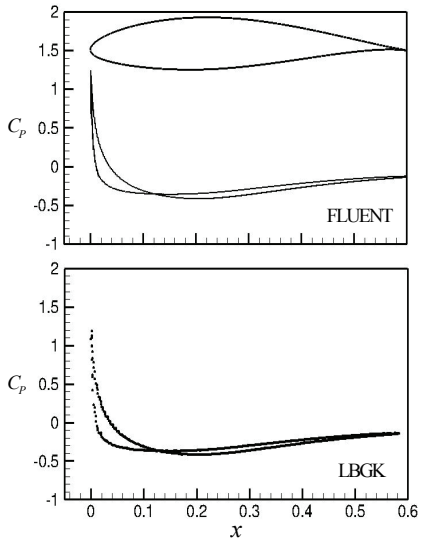

Fig. 8 C_p distribution along the chord of clean NACA63-415 at $\mathrm{Re} = 500$, $\alpha = 0°$.

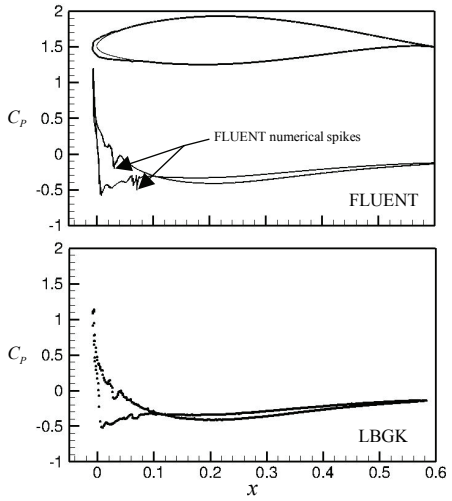

Fig. 9 C_p distribution along the chord of ice-accreted section number 1 of NACA63-415 at $\mathrm{Re} = 500$, $\alpha = 0°$.

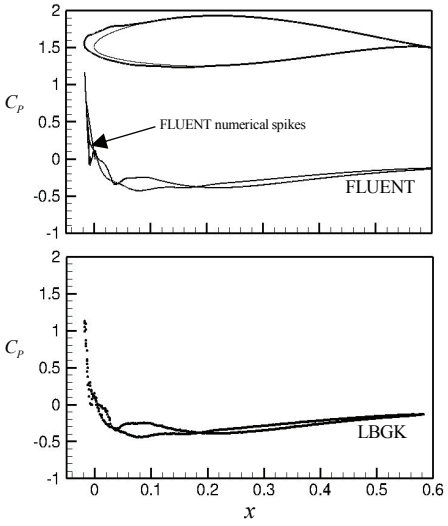

Fig. 10 C_p distribution along the chord of ice-accreted section number 2 of NACA63-415 at $\mathrm{Re} = 500$, $\alpha = 0°$.

Concerning the values of C_d and C_l obtained under steady state conditions and summarized in Table 4, a very good agreement is found for the drag coefficient while some discrepancies are observed in the lift parameter. As already mentioned, the impossibility of correctly handling irregular surfaces produces a smoothness of macroscopic quantities which may lead to differences on the computed coefficients. Note that C_d coefficients obtained with both methods are identical for clean airfoils and only a minor discrepancy is observed when ice is present. This behaviour is similar to the one previously found for the pressure coefficient. In turn, a comparison of calculated lift coefficients with $\alpha = 0°$ is more

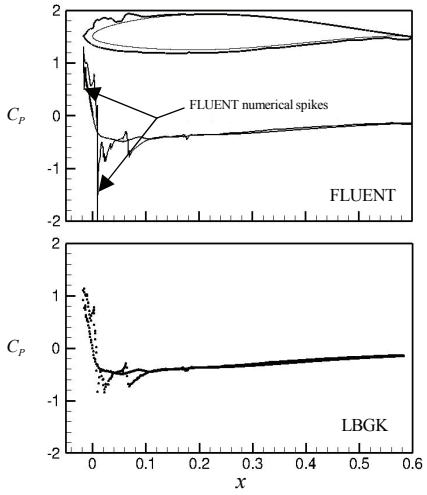

Fig. 11 C_p distribution along the chord of ice-accreted section number 3 of NACA63-415 at $\mathrm{Re} = 500$, $\alpha = 0°$.

cumbersome to analyse. In fact, for this angle of attack the values are very small; thus, error analyses can bring about higher relative errors.It is obvious that these errors must be less significant with increasing the absolute value of C_l. As shown in Table 5, the difference between C_l values calculated with FLUENT and the LBGK method, for $\alpha = 8°$ are quite similar.

After these tests for stationary flows, the study of the unsteady flow over the profile inclined at $\alpha = 28°$ was carried out using a similar domain with a refinement factor of $m = 4$, the corresponding relaxation times are $\tau_c = 0.5075$, $\tau_1 = 0.53$ and $\tau_2 = 0.62$ .A test on a clean airfoil was first performed to determine the capabilities of the proposed methodology to handle unsteady separated flows. Although not fully equivalent, this test was found necessary prior to the study of separation triggered by ice accretion at the leading edge. As in previous cases, the results computed with the LBGK program are compared with numerical solutions obtained with FLUENT. The evolution of C_d and C_l obtained with the current method and with FLUENT is shown in Fig. 12 for the clean profile and Fig. 13 for the ice-accreted section number one (depicted in Fig. 9). Periodic oscillations of the coefficients express the regular formation and release of vortices in the wake of the profile (Fig. 14).

For this unsteady case, both methods give a quite similar time evolution of characteristic coefficients. They are of the same magnitude, follow a similar regular release of vortices and with closer examination, as at $\alpha = 0°$, ice accretion induces an increase in drag and lift. Table 6 compare the

Table 4 Aerodynamic coefficients for flow around clean and several sections of ice-accreted NACA63-415 at $\mathrm{Re} = 500$, $\alpha = 0°$.

Cases	Methods	C_d	C_l	C_d difference	C_l difference
Clean 0°	FLUENT LBGK	0.1809 0.1809	-0.0057 -0.0045	 0 %	 21 %
Ice-accreted section 1 0°	FLUENT LBGK	0.1820 0.1823	-0.0072 -0.0173	 0.16 %	 140 %
Ice-accreted section 2 0°	FLUENT LBGK	0.1830 0.1837	0.009 -0.0005	 0.4 %	 105 %
Ice-accreted section 3 0°	FLUENT LBGK	0.1919 0.1925	0.0193 0.0178	 0.31 %	 7.7 %

Table 5 Aerodynamic coefficients for flow around clean NACA63-415 airfoil at $\mathrm{Re} = 500$, $\alpha = 8°$.

Cases	Methods	C_d	C_l	C_d difference	C_l difference
Clean 8°	FLUENT LBGK	0.2022 0.2022	0.3622 0.3558	 0 %	 1.8 %

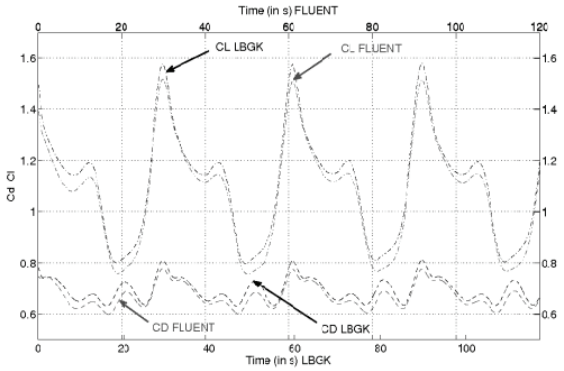

Fig. 12 Unsteady drag and lift coefficients on the clean NACA63-415 at $\mathrm{Re} = 500$, $\alpha = 28°$.

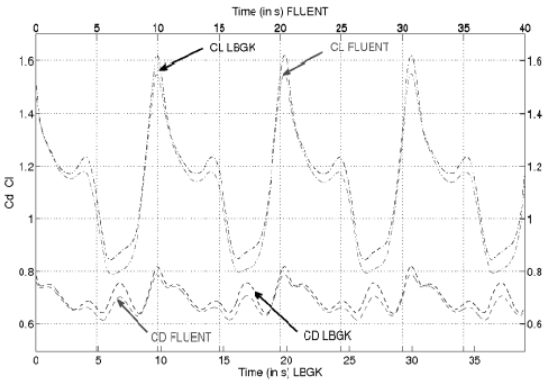

Fig. 13 Unsteady drag and lift coefficients on the ice-accreted section 1 of NACA63-415 at $\mathrm{Re} = 500$, $\alpha = 28°$.

periods predicted by the lattice Boltzmann and Navier-Stokes approaches. It is noted that for this case there is a geometric factor of 3 regarding the length of the physical cord on the clean ($C = 0.6\ m$) and the ice-accreted ($C = 0.6\ m$) profiles. This has naturally a direct influence on the time length the time length on the period of oscillations.

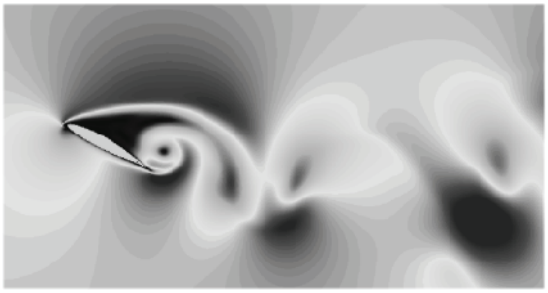

Fig. 14 Vortex development behind the NACA63-415 airfoil at $\mathrm{Re} = 500$, $\alpha = 28°$.

Despite the differences in the model, the calculation method, and the gridding, it is encouraging to find that the study of the NACA63-415 profile with LBGK and NS solvers provides results which show good agreement under both steady and unsteady conditions.

4. CONCLUSIONS

A basic LBGK algorithm has been implemented, along with the following improvements; multiple gridding approach and curved boundary treatment. The resulting computational program was validated by simulating laminar flows at low Reynolds numbers on a test case regarding a staggered bundle of tubes and over a NACA63-415 airfoil under clean and ice-accreted conditions. Numerical predictions were compared with results obtained with Navier-Stokes solver FLUENT using finite volume formulation. For both applications, the lattice Boltzmann method and the Navier-Stokes based solver showed very similar results.

The test over the bundle of tubes allowed to verify that multiple embedded grids and treatment for curved boundaries were implemented adequately.

Table 6 Period of the oscillations around clean and ice-accreted NACA63-415 at $\mathrm{Re} = 500$, $\alpha = 8°$.

Methods	Period [seconds] clean profile	Period [seconds] iced profile
FLUENT	31 s	10.4 s
LBGK	30.3 s	10.1 s
% difference	2.25 %	2.88 %

This case showed the direct impact of the compressibility limit on the solution accuracy.

For the NACA profile, good predictions of the influence of ice accretion at the leading edge of the airfoil were also obtained. With a simple gridding, the LBGK method is shown to be an alternative to classical NS solvers, mostly due to the intrinsic unsteady character of the method. This was verified for the flow over the airfoil under clean and ice-accreted conditions for an angle of attack $\alpha = 28°$. The computed evolution of unsteady lift and drag coefficients agreed very well with the solution obtained via FLUENT.

Now that the ability of the LBGK method to simulate laminar flows around NACA airfoils has been shown, the next step will be flow simulation at high Reynolds numbers, especially regarding turbulence. Another possible evolution concerns the flexibility of the method towards additional physics. In fact, thanks to the fundamental mesoscopic approach of the method, with particular distribution functions devoted to thermal problems and multiphase flows, it should be possible to predict ice formation and ice impact in a single simulation. (The Matlab computational code used in this study is available on demand.)

REFERENCES

1. Bhatnagar PL, Gross EP, Krook M (1954). A model for collision processes in gases. I. Small amplitude processes in charged and neutral one-components systems, *Phys. Rev.* 94(3):511–525.
2. Chen S, Chen H, Martinez D, Matthaeus W (1991). Lattice Boltzmann model for simulation of magnetohydrodynamics, *Phys. Rev. Lett.* 67(27):3776–3779.
3. Dupuis A, Chopard B (2003). Theory and applications of an alternative lattice Boltzmann grid refinement algorithm, *Phys. Rev. E* 67(6):066707.
4. Etienne S, Garon A, Pelletier D (2009). Perspective on the geometric conservation law and finite element methods for ALE simulations of incompressible flow, *J. Comput. Phys.* 228(7):2313–2333.
5. Filippova O, Hänel D (1998). Grid refinement technique for lattice-BGK models, *J. Comput. Phys.* 147(1):219–228.
6. He X, Luo L (1997). Theory of the lattice Boltzmann method: from the Boltzmann equation to the lattice Boltzmann equation, *Phys. Rev. E* 56(6):6811–6817.
7. Koelman JMVA (1991). A simple Boltzmann scheme for Navier-Stokes fluide flow, *Europhys. Lett.* 15(6):603–607.
8. Latt J, Chopard B, Malaspinas O, Deville M, Michler A (2008). Straight velocity boundaries in the lattice Boltzmann method, *Phys. Rev. E* 77(5):056703.
9. Mei R, Luo L-S, Shyy W (1999). An accurate curved boundary treatment in the lattice Boltzmann method, *J. Comput. Phys.* 155(2):307–330.
10. Mei R, Yu D, Shyy W (2002). Force evaluation in the lattice Boltzmann method involving curved geometry, *Phys. Rev. E* 65(4):041203.
11. Qian YH, D'Humieres D, Lallemand P (1992). Lattice BGK models for Navier-Stokes equation, *Europhys. Lett.* 17(6):479–484.
12. Rohde M, Kandhai D, Derksen JJ, Van den Akker HEA (2006). A generic, mass conservative local grid refinement technique for lattice Boltzmann schemes, *Int. J. Numer. Meth. Fluid* 51(4):439–468.
13. Succi S (2001). *The Lattice Boltzmann Equation for Fluid Dynamics and Beyond,* Oxford University Press.
14. Watteaux R (2008). *Étude des facteurs d'influence d'un faisceau de cylindres dans un écoulement transverse à bas régime,* Master's thesis, École Polytechnique de Montréal.
15. Wolf-Gladrow DA (2000). *Lattice-Gas Cellular Automata and Lattice Boltzmann Models: an Introduction,* Springer, Berlin.